Dimeric assembly of F_1-like ATPase for *Mycoplasma* gliding motility

Takuma Toyonaga[1,2], Takayuki Kato[3], Akihiro Kawamoto[3], Tomoko Miyata[4,5], Keisuke Kawakami[6], Junso Fujita[4,5,7], Tasuku Hamaguchi[8], Keiichi Namba[4,5], Makoto Miyata[1,2]*

[1]Graduate School of Science, Osaka Metropolitan University, 3-3-138 Sugimoto, Sumiyoshi-ku, Osaka 558-8585, Japan.

[2]The OCU Advanced Research Institute for Natural Science and Technology (OCARINA), Osaka Metropolitan University, 3-3-138 Sugimoto, Sumiyoshi-ku, Osaka 558-8585, Japan.

[3]Institute for Protein Research, Osaka University, 3-2 Yamadaoka, Suita, Osaka, 565-0871, Japan.

[4]Graduate School of Frontier Biosciences, Osaka University, 1-3 Yamadaoka, Suita, Osaka, 565-0871, Japan.

[5]JEOL YOKOGUSHI Research Alliance Laboratories, Osaka University, 1-3 Yamadaoka, Suita, Osaka, 565-0871, Japan.

[6]Biostructual Mechanism Laboratory, RIKEN, SPring-8 Center, 1-1-1, Kouto, Sayo, Hyougo, 679-5148, Japan.

[7]Graduate School of Pharmaceutical Sciences, Osaka University, 1-6 Yamadaoka, Suita, Osaka, 565-0871, Japan.

[8]Institute of Multidisciplinary Research for Advanced Materials, Tohoku University, 2-1-1 Katahira, Aoba-ku, Sendai, 980-8577, Japan.

*Corresponding author. Email: miyata@omu.ac.jp

Abstract

Rotary ATPases, including F_1F_o- and V/A-ATPases, are molecular motors that perform rotational movements for energy conversion[1]. In the gliding bacterium *Mycoplasma mobile*, a dimeric F_1-like ATPase forms a chain structure with the glycolytic enzyme, phosphoglycerate kinase (PGK), within the cell[2]. This unique dimeric ATPase has been proposed to drive the gliding motility[2–4]. However, the mechanisms underlying force generation and transmission remain unclear. Here, we present a 3.2 Å resolution structure of the dimeric ATPase complex obtained by electron cryomicroscopy (cryo-EM). The structure revealed an assembly distinct from the known dimeric forms of F_1F_o-ATPase[5] despite containing conserved F_1-ATPase structures. The two ATPase units are interconnected by GliD dimers, which were previously identified as MMOB1620[2,6]. Gliβ, a homologue of the F_1-ATPase catalytic subunit[6], displays a specific N-terminal region that incorporates PGK into the complex. ATPase shows strong similarities to F_1-ATPase in terms of the structural conformations of the catalytic subunits, catalytically important residues, and the nucleotide-binding pattern of the catalytic sites, suggesting a rotation based on the rotary catalytic mechanism conserved in rotary ATPases[1,7–10]. The cryo-EM structure underscores the evolutionary connection in rotary ATPases and provides insights into the mechanism by which F_1-like ATPases drive bacterial gliding motility.

Introduction

Rotary ATPases are molecular motors that link ATP hydrolysis or synthesis to ion transport via rotational motion in biological membranes[1]. These motors comprise two common domains: soluble R_1, which is responsible for ATP hydrolysis and synthesis,

and membrane-embedded R_o, which is responsible for ion transport. F_1F_o-ATPase, a rotary ATPase conserved across most eukaryotes, archaea, and bacteria, is responsible for ATP synthesis and the maintenance of membrane potential[5]. In four mycoplasma species, *Mycoplasma mobile*, *Mycoplasma pulmonis*, *Mycoplasma agassizii*, and *Mycoplasma testudineum*, an F_1-like ATPase gene cluster, referred to as Type 2 ATPase, is present, in addition to the genuine F_1F_o-ATPase gene cluster, referred to as Type 1 ATPase[11,12] (Extended Data Fig. 1). The presence of F_1-ATPase α and β subunit homologues (MMOBs 1660 and 1670 in *M. mobile*) in the Type 2 ATPase gene cluster suggests a shared evolutionary origin in the F_1 domain. Type 2 ATPases have been proposed to drive the gliding motility observed in *M. mobile* and *M. pulmonis*[2–4,13,14]. *M. mobile*, a fish pathogen, glides at a speed of up to 4 µm per second on a solid surface covered with sialylated oligosaccharides which is found on host cell surfaces[15] (Fig. 1a, Extended Data Fig. 2). In our proposed model of gliding, filamentous leg structures on the mycoplasma cell surface, which are approximately 50 nm long, propel the cell body by catching and pulling sialylated oligosaccharides on the solid surface. Inside the cell, motors composed of Type 2 ATPase and phosphoglycerate kinase (PGK), which converts ADP to ATP during glycolysis, are linked near the cell membrane to form "internal chains"[2,6]. The motor is composed of dimerized F_1-like ATPase units with unique bridge structures, hence referred to as twin motor. However, the mechanisms underlying force generation and transmission remain unclear. In this study, we elucidated the detailed structure of a twin motor using cryo-EM single-particle analysis (SPA). The structural features show strong homology to F_1-ATPase[7,8], suggesting a rotary catalytic mechanism homologous to that of rotary ATPases[1,9,10] for *M. mobile* gliding motility.

Results

Protein identification in cryoEM structure of twin motor

We performed cryo-EM SPA of the twin motors isolated from *M. mobile* cells, using images collected on an epoxidized graphene grid (EG grid)[16] (Extended Data Table 1). The overall 3D structure of the twin motor was determined at 3.2 Å resolution (Fig. 1b, Extended Data Figs. 3 and 4). Local refinement improved the resolution of the regions, each containing an F_1-like ATPase unit, to 3.1 Å (Extended Data Figs. 3b and 4). Density maps enabled the construction of an atomic model of the twin motor (Fig. 1c). The modelled sequences of each subunit are summarised in Extended Data Table 2. The twin motor exhibits a rectangular structure with dimensions of approximately 350 Å × 250 Å × 150 Å and contains at least 24 polypeptide chains with a total mass of ~1.5 MDa. The structure revealed that the two F_1-like ATPase units are inclined towards each other by ~5° and form a dimer with pseudo-two-fold rotational symmetry along with several accessories (Fig. 1c,d). F_1-like ATPase is composed of a hexameric ring of two alternating subunits and a central shaft subunit, identified as MMOBs 1660, 1670, and 1630, respectively. We named them Gliα, Gliβ, and Gliγ, following the subunit names of F_1-ATPase[10]. In the hexameric ring, nucleotide-derived densities are observed at five of the six subunits interfaces, even though the samples were isolated and analysed under nucleotide-free conditions, indicating that it contained endogenous nucleotides, as reported for F_1-ATPase[17] (Fig. 1c,e). The subunit attached to Gliα and forming a "bridge" between two F_1-like ATPase units was identified as MMOB1620, and we named it GliD (Fig. 1c). The three densities protruding from the dimeric F_1-like ATPase were identified as MMOB4530, annotated as PGK. The denoised 3D map showed additional distinct

densities at six locations, including the $PGK_{1–3}$ regions (Extended Data Fig. 5a). These six densities showed correlation coefficients from 0.37 to 0.48 with the crystal structure of PGK from *Staphylococcus aureus* (PDB ID: 4DG5) (Extended Data Fig. 5b,c). These assignments are consistent with the stoichiometry previously estimated by sodium dodecyl sulfate-polyacrylamide gel electrophoresis (SDS-PAGE)[2]. A protein density bound to only one of the two F_1-like ATPase units was identified as MMOB3660, which was newly detected by SDS-PAGE of the twin motor, and we named this GliE (Fig. 1b,c, Extended Data Fig. 6). This small protein (112 aa), characterised by a β-sandwich, was nestled between the ATPase hexamer and other subunits, breaking the rotational symmetry of the complex (Extended Data Fig. 7). Although MMOB1640, encoded in the Type 2 ATPase gene cluster, was detected by SDS-PAGE of the twin motor (Extended Data Fig. 6), the protein density was not observed in the overall 3D map.

Structural features of subunits comprising F_1-like ATPase

Gliβ and Gliα exhibit high structural similarity to the β and α subunits of the F_1-ATPase from the thermophilic bacterium *Bacillus* PS3 (PDB ID: 8HH5), as demonstrated by the superimposition of their Cα atoms with the root mean squared deviations (r.m.s.d.) of 1.95 Å and 2.79 Å, respectively (Fig. 1g,i). Both Gliβ and Gliα possess three domains: crown, nucleotide-binding domain (NBD), and C-terminal domain (CTD). The NBDs of Gliβ and Gliα are featured with a phosphate-binding motif of P-loop[18], consisting of the amino acid sequences GGAGVGKT and GDRGTGKT, respectively (Fig. 1f,h). The Gliβ-CTD contains a DELSEED loop, important for torque transmission in the F_1-ATPase β subunit[19], with an amino acid sequence of DALSEDD (Fig. 1f). A striking difference of Gliβ from the F_1-ATPase β subunit is the presence of an extended

N-terminal region consisting of the N-terminal domain (NTD) and linker (Fig. 1f, Extended Data Fig. 8a). This region comprises approximately 100 residues located within the extra N-terminal 299 residues of Gliβ, in comparison to the F_1-ATPase β subunit[6,12]. The linker hangs outside the F_1-like ATPase along the crown and NBD (Extended Data Fig. 8b). Gliβ-NTDs, consisting of 4 to 6 helices, are oriented in various directions among Gliβs, depending on their position in the complex (Extended Data Fig. 8a,c,d). Gliβ-NTD interacts with PGK (Fig. 2a,b). In addition, at the interface of the two F_1-like ATPase units, the N-terminal regions of $Gli\beta_3$ and $Gli\beta_6$ interact with the NBDs of $Gli\alpha_6$ and $Gli\alpha_3$ of another F_1-like ATPase unit, respectively (Fig. 2a,c). These interactions suggest that the Gliβ-specific N-terminal region has been acquired for the incorporation of PGK into the twin motor and for the stabilisation of the ATPase dimer. A difference of Gliα from the F_1-ATPase α subunit is the absence of the H1 helix, which interacts with the peripheral stalk[20] (Extended Data Fig. 9). This is consistent with the lack of a gene homologous to the peripheral stalk in the Type 2 ATPase gene cluster[12]. Gliγ, composed of a coiled-coil and an α/β fold typical of the F_1-ATPase γ subunit, can be superimposed on the γ subunit of the *Bacillus* PS3 F_1-ATPase with an r.m.s.d. of 5.79 Å for Cα atoms due to lower sequence conservation than the catalytic subunits[15] (Fig. 1j,k). The folded C-terminal α-helix, which is 25 Å longer than the F_1-ATPase γ subunit, protrudes from the N-terminal side of the hexameric ring and interacts with the crowns of Gliαβ (Fig. 1k, Extended Data Fig. 10a,b). The coiled coil of Gliγ hydrophobically interacts with the CTDs of Gliαβ in the hexameric ring (Extended Data Fig. 10c). In F_1-ATPase, this interaction has been reported to be involved in axle hold and torque transmission[21].

Accessories of dimeric F_1-like ATPase

Generally, PGK is bifurcated into two domains interconnected by an α-helix: the NTD, which binds to 3-PG or 1,3-BPG, and the CTD, which binds to Mg-ADP or Mg-ATP[22] (Extended Data Fig. 11a). The twin motor PGK structure, containing the CTD and a segment of the α-helix, exhibits high structural similarity to the PGK from *Staphylococcus aureus* (PDB ID: 4DG5), with an r.m.s.d. of 3.12 Å for Cα atoms (Extended Data Fig. 11a–c). The β loop of the PGK-CTD invades the depression of the folded Gliβ-NTD and interacts with the H2 helix and the H2–H3 loop of the Gliβ-NTD (Fig. 2d). The H4–β loop and the H5 helix of the PGK-CTD also interact with the H5 and H4 helices of the Gliβ-NTD, respectively. Nucleotide-derived densities are not found in the PGK-CTD of the twin motor, even though residues important for nucleotide binding in the PGK are conserved[23] (Extended Data Fig. 11d–f,12). None of the twin-motor PGK-NTDs were modelled because of the poor density of the reconstruction (Extended Data Fig. 11b). However, the binding and catalytic residues of 3-PG or 1,3-BPG in PGK are conserved in the amino acid sequence, suggesting that the twin-motor PGK possesses enzymatic activity (Extended Data Fig. 12). Given that the binding and catalytic residues are not conserved in another PGK homologue, MMOB4490, encoded in the *M. mobile* genome, the twin-motor PGK is likely to function as the original PGK during glycolysis (Extended Data Fig. 12). GliD ($GliD_{1,3,4,6}$) bridge components form dimers at the interface of two F_1-like ATPase units, whereas $GliD_{2,5}$ exists as monomers at the twin-motor end (Fig. 2a,e,f). GliD is characterised by a globular domain and an N-terminal long α-helix (H2), which is only visualised in the dimer. The globular domain interacts with the H20–H25 region at the C-terminus of Gliα (Fig. 2g,h). The two H2 helices in the GliD dimer are aligned

parallel to each other across the H20–H25 region of Gliα, GliE, Gliβ-NTD, and Gliβ-CTD (Fig. 2f). These two α-helices are reminiscent of the dynein buttress that connects the AAA+ ring and the tubulin-binding domain[24], suggesting a regulatory role for structural changes induced by the ATPase activity of the F_1-like ATPase units.

Structural information suggesting a catalytic mechanism homologous to F_1-ATPase

The crown region of the hexameric ring exhibits nearly six-fold rotational symmetry, whereas the CTD region displays asymmetry (Extended Data Fig. 10a). This observation suggests a structural change with a pivotal point between the crown and CTD. $Gli\beta_{1–3}$ adopt three distinct conformations, which appear to be the transition states of CTD flexion motion toward Gliγ, with a positional difference of the DELSEED loop by 11 Å (Fig. 3a). We named these conformations $Gli\beta_C$ (closed), $Gli\beta_{HO}$ (half-open), and $Gli\beta_O$ (open), following the conformation names of F_1-ATPase[8]. They are arranged clockwise when viewed from the C-terminus of the hexameric ring (Fig. 3b). These conformations resemble the states referred to as *ATP-waiting* or *step-waiting*, the latter of which occurs after ATP binding, during the catalytic reaction of *Bacillus* PS3 F_1-ATPase[8] (Extended Data Table 3). In Gliα, the region corresponding to the DELSEED loop shows only a 5 Å difference in position relative to the Gliγ side, while the H20–H25 region interacting with GliD shows a 9 Å difference (Extended Data Fig. 13). We named these conformations $Gli\alpha_C$ (close), $Gli\alpha_{HO}$ (half-open), and $Gli\alpha_O$ (open) based on the H20–H25 positions viewed from the Gliγ side. If this difference in Gliα represents a conformational change associated with ATP hydrolysis of the twin motor, it implies force transfer from F_1-like ATPase to GliD. The catalytic sites formed at the α-β interface of $Gli\alpha_C\beta_C$ and $Gli\alpha_{HO}\beta_{HO}$ contain Mg-ATP and Mg-ADP+P_i, respectively,

while no nucleotide density is found at the catalytic site of Gli$\alpha_O\beta_O$ (Fig. 3b–d, Extended Data Fig. 14). Nucleotide-binding states are also shared between the two F_1-like ATPases, according to the pseudo-two-fold rotational symmetry. The residues of F_1-ATPase involved in ATP hydrolysis, including those in the arginine finger, are conserved in Gli$\alpha\beta$, suggesting a shared ATP hydrolysis pathway between F_1-ATPase and the twin motor (Fig. 3d). The Mg-ATP was observed at the remaining three interfaces, hereafter referred to as the β-α interfaces (Fig. 3b, Extended Data Fig. 14). At the β-α interface, Gliα-K179 corresponds to the position of conserved residue Q200 of the F_1-ATPase α subunit (Extended Data Fig. 15a,b). Compared to the α-β interface, Gliα-K179 is charge inverted relative to the glutamate essential for the catalytic activity (E190 of F_1-ATPase β subunit), suggesting that the β-α interface, akin to F_1-ATPase, has no ATP hydrolytic activity (Extended Data Fig. 15c). The conformational sequence pattern of three Gliβ subunits with nucleotide bound is identical to that of the *ATP-waiting* state of the F_1-ATPase[8]. These data suggest that the Mg-ATP binding to the catalytic site of Gli$\alpha_O\beta_O$ promotes the catalytic reaction of the entire F_1-like ATPase based on the catalytic mechanism analogous to that of F_1-ATPase.

Motors in the chain

The atomic model of the twin motor was fitted to the previously reconstructed density of the internal chain obtained using negative-staining electron microscopy SPA[2] (Fig. 4a). To circumvent misfitting of the long-axis orientation of the twin motors due to the low-resolution density map (29.7 Å) of the chain structure, regions with asymmetric structures, such as the NTDs of Gli$\beta_{3,6}$, GliE, and PGK_3, were excluded. At the interface between the twin motor units, GliDs that project along the long axis of the twin motors

face each other, suggesting their role as linkers for chain formation. However, the 3D map of the chain has remaining density at the interface that cannot be filled by GliDs. This density may correspond to 100 unmodelled N-terminal residues and the loop of GliD.

Discussion

The major difference of the twin motor from the dimeric form of eukaryotic mitochondrial ATP synthases[5] is the interaction in the F_1 region only, via GliD and the N-terminal region of Gliβ. Although the GliD dimer does not have a transmembrane segment, the two long α-helices at the N-terminus are reminiscent of the structure of a peripheral stalk. This observation is consistent with the hypothesis that the MMOB1620 gene encoding GliD is derived through gene fusion from the b and δ subunits, which comprise the peripheral stalk[15]. GliD-mediated dimer and chain formation may allow F_1-like ATPase units to work cooperatively. In support of this, changes in the distance between the twin motors have been reported to be associated with the ATP hydrolysis reaction, suggesting force transfer between the twin motors through GliD[3,4]. PGK in the twin motor may efficiently supply ATP to ATPase as fuel. Furthermore, PGK molecules protruding from the transverse axis of the motor may be involved in sheet formation in the internal chain, as observed by negative-staining EM[25]. The weak density of PGK in the cryo-EM map can be explained by the flexibility suggested by the high-speed atomic force microscopy[2]. The flexibility of the PGK molecule suggests that the chain sheet serves as a cytoskeleton to withstand mechanical stress in mycoplasma cells, which are characterised by the absence of a cell wall. The GliE subunit, which is bound to only one side of the dimeric F_1-like ATPase, creates an asymmetry in the twin motor

structure and may contribute to the unidirectional nature of gliding motility. However, we cannot rule out the possibility that this protein also binds to another side of the dimeric F_1-like ATPase in the cell and was dislodged during purification.

The three distinct forms of the catalytic subunit Gliβ and their corresponding nucleotide binding suggest a rotary catalytic mechanism analogous to that of the rotary ATPases (Fig. 4b). In this rotary catalytic mechanism, $Gli\alpha_O\beta_O$ transitions to $Gli\alpha_C\beta_C$, during which the DELSEED loop of Gliβ approaches Gliγ upon ATP binding at the catalytic site. The other Gliαβ dimers in the hexameric ring also operate cooperatively, with $Gli\alpha_C\beta_C$ transitioning to $Gli\alpha_{HO}\beta_{HO}$ upon ATP hydrolysis and $Gli\alpha_{HO}\beta_{HO}$ transitioning to $Gli\alpha_O\beta_O$ upon ADP and phosphate release. This one-step conformational change of the hexameric ring prompts a 120-degree rotation of Gliγ. Each Gliαβ dimer sequentially hydrolyses ATP, and through three steps, the hexameric ring structure and the position of Gliγ revert to their initial states. The pseudo-two-fold rotational symmetry structure of the twin motor suggests that the two F_1-like ATPase units operate in a synchronised manner while maintaining structural symmetry. Throughout the catalytic reaction, significant changes in the positioning of the two F_1-like ATPase units within the twin motor may be hindered due to the presence of the N-terminal regions of Gliβ bridging the two units and a buttress-like structure composed of two long α-helices of the GliD dimer (Fig.2a,c,f).

For cell gliding, the rotary motion of the twin motors must be converted into linear motion. One possible explanation for this conversion mechanism is that the membrane protein Gli521, which consists of a hook and a rod, functions as a crank[26] (Fig.4c).

Upon conversion of rotary to linear motion, Gli521 pulls the leg protein Gli349, which is bound to sialylated oligosaccharides on the host cell surface, thereby propelling the mycoplasma cells forward[27]. The presence of a globular domain in Gliγ, similar to that in the F_1-ATPase γ subunit, suggests a potential interaction with a membrane-embedded F_o-like domain. MMOB1610 and MMOB1650, encoded by the Type 2 ATPase gene cluster, possess 12 and two transmembrane segments, respectively[15]. These two proteins are potential partners for the globular domain of Gliγ to interact with at the cell membrane, transmitting the rotary motion to Gli521 on the cell surface.

The role of twin motors diverges from that of rotary ATPases and their relatives, such as the flagellar type III protein export apparatus, which exhibit a hexameric ring with a central shaft and are involved in protein and ion transport[28,29]. We hypothesised that the F_1F_o-ATPase acquired the role and mechanism of the twin motor through incidental contact with an adhesin on the membrane during the evolution of mycoplasma from a non-motile to a motile state[2,30]. This primitive gliding motility would have conferred a survival advantage. Another F_1-like ATPase, referred to as Type 3 ATPase, has also been found in mycoplasmas and may drive the system that cleaves host antibodies[12,31]. Types 2 and 3 ATPases have a commonality in that they transitioned from F_1-ATPase to mechanisms that drive mycoplasma-specific systems. Understanding these unique F_1-like ATPases will contribute to the study of the working principles and evolution of rotary ATPases.

Materials and Methods

Optical microscopy

Cells of the *Mycoplasma mobile* mutant strain (gli521[P476R]), which can glide as the wild-type strain but binds to sialylated oligosaccharides more tightly, were cultured, observed using phase-contrast microscopy, and recorded as previously described[32–35]. The recorded video was analysed using the ImageJ software, version 1.54d (https://imagej.nih.gov/ij/).

Isolation of twin motor

The twin motor was isolated from *Mycoplasma mobile* mutant strain (gli521[P476R]) as described previously[2]. The twin-motor preparation was concentrated to 1 mg/ml using a 100 K Vivaspin concentrator (Merck, Germany) with 0.1% (w/v) 3-[(3-cholamidopropyl)-dimethyl-ammonio]-1-propanesulfonic acid (CHAPS) to prevent membrane adsorption. The concentrated motor was applied to SDS-PAGE and stained with Coomassie brilliant blue R-250. The bands of the component proteins were identified using peptide mass fingerprinting, as described previously[36].

Cryo-EM grid preparation and data acquisition

The EG grid was prepared as described previously[37]. A 2.6 μl sample solution was applied onto the grid and automatically blotted from both sides using a filter paper at 4 °C for 2 s in 100% humidity, and vitrificated using a semi-automated vitrification device, Vitrobot Mark IV (Thermo Fisher Scientific, USA). Cryo-EM imaging was performed using CRYO ARM 300 (JEOL, Japan) operated at 300 kV with a K3 direct electron detector camera (AMETEK, Gatan, USA). A total of 7,350 movies were recorded using SerialEM software[38] with a total dose of about 80 electrons $Å^{-2}$ for 40 frames, an exposure time of 3.3 sec per movie and a nominal defocus range from −0.8

to −1.8 μm. The nominal magnification was ×60,000 corresponding to 0.87 Å per pixel.

Cryo-EM image processing

The image-processing steps for SPA are summarised in Extended Data Figs. 3 and 4. Image processing was performed using cryoSPARC v3.3.2,[39] unless otherwise stated. The movies were aligned using patch-based motion correction, and the contrast transfer function (CTF) parameters were estimated using Patch CTF estimation. Micrographs with CTF fit resolution worse than 8 Å were removed. Particles were automatically picked up by Blob Picker, extracted with ×4 binning and subjected to 2D-classification. The obtained 2D averaged images were used as templates for the template picker to pick up good particles. After two rounds of 2D classification, the selected particles were subjected to local motion correction and reextracted using the original pixel size. The particles were subjected to Ab-initio reconstruction using C1 symmetry enforced with a final resolution limit of 12 Å and, heterogeneous reconstruction with 3 classes. Particles in class 2 were subjected to homogeneous reconstruction using C1 symmetry, resulting in a map at a resolution of 3.5 Å. The final map was generated by local and global CTF refinement, and then non-uniform refinement. To improve the local resolution, the final map and particles were subjected to particle subtraction and local refinement using C1 symmetry to generate half-divided maps, each containing a monomeric ATPase. The entire map and two local maps were subjected to mask creation and postprocessing in RELION 4.0[40], resulting in resolutions of 3.2, 3.1, and 3.1 Å, respectively. Local resolution estimation was performed using the RELION 4.0. The post-processed map was denoised using the Topaz software version 0.2.5 with the trained model Unet-3d-10a[41]. Calculation of the Fourier shell correlation (FSC) curve

between the two half-maps and estimation of the local resolution were performed using RELION 4.0.

Modelling

Initial models for GliαβγDE were generated using AlphaFold2[42], while the homology model for PGK was generated using Modeller version 10.4[43] with the atomic model of PGK (PDB ID: 4DG5) from *Staphylococcus aureus*. The generated models were fitted to the corresponding densities of the EM map as rigid bodies using the UCSF Chimera version 1.15[44]. The fitted models were manually inspected and adjusted using COOT version 0.9.8.1,[45] and refined using the *phenix.real_space_refine* program in PHENIX version 1.19[46,47] with reference model restraints using the atomic models of ATP synthase (PDB ID: 5IK2) from *Caldalaklibacillus thermarum*, and PGK (PDB ID: 3ZLB) from *Streptococcus pneumoniae*. Manual adjustments using COOT and refinement using PHENIX were repeated until the model parameters no longer improved. The FSC curves between the map and the model were calculated using PHENIX. The refined model was also evaluated by a comprehensive validation of the PHENIX and Q-scores[48]. To identify the nucleotide-binding sites of F_1-like ATPases, F_o - F_c maps were generated using Servalcat[49]. Superposition of models and fitting of them to the map were performed using UCSF ChimeraX version 1.2.5[50]. All structural figures were rendered using UCSF ChimeraX.

Data availability

The cryo-EM map for the twin motor is now under deposition in the Electron Microscopy Data Bank (EMDB). The coordinates are now under deposition in the

Protein Data Bank (PDB).

Fig. 1 Structure of the twin motor featuring dimeric F_1-like ATPase.

(**a**) Gliding machinery of *Mycoplasma mobile*. The overall view of the gliding machinery (top) and a part of the internal chain (bottom) are depicted. (**b**) Overall structure of the twin motor. The scale bar indicates 5 nm. The cartoon is drawn in the upper left region. (**c**) Atomic model of the twin motor. Nucleotides are indicated by black triangles. The maps in (b) and (c) are contoured at 0.55 in UCSF ChimeraX. (**d**) Dimeric F_1-like ATPase in the twin motor. Dotted lines indicate the axis of each ATPase. (**e**) Density of Mg-ATP bound to F_1-like ATPase. The dotted region in (c) is shown. (**f,h,j**) Subunits constituting F_1-like ATPase. (**g,i,k**) Overlay of subunits of F_1-like ATPase and *Bacillus* PS3 F_1-ATPase. The subunits of the *Bacillus* PS3 F_1-ATPase, αβ (PDB ID: 8HH5) and γ (PDB ID: 8HH2), are coloured in purple.

Fig. 2 Interaction between subunits.

(**a**) N-terminal and C-terminal regions of the twin motor. The twin motor is viewed from the top of the cartoon. Arrows indicate the interface between the dimeric F_1-like ATPases. The maps in (a) are contoured at 0.55 in UCSF ChimeraX. (**b**) Structure of Gliβ and PGK. (**c**) Interaction between the N-terminal region of Gliβ and Gliα-NBD at the interface between dimeric F_1-like ATPases. The dotted region in (a) is shown. (**d**) Interaction of PGK with the Gliβ-NTD. The dotted region in (a) is shown. (**e**) Structure of Gliα and GliD monomer. (**f**) GliD dimer at the interface between dimeric F_1-like ATPases. The right figure corresponds to the dotted region in the cartoon. (**g,h**) Interaction between GliD and Gliα-CTD. Each corresponds to the dotted regions in (f).

Fig. 3 Structural conformations and nucleotide binding of Gliβ.

(**a**) Differences in the conformations of the three Gliβ. Three Gliβs in the F_1-like ATPase are superposed. The dotted lines indicate the position of the DELSEED loop of each Gliβ. (**b**) Nucleotide-binding pattern of dimeric F_1-like ATPase and F_1-ATPase. The catalytic site is circled by black dotted lines. (**c**) Gliαβ dimer in each conformation in the hexamer. (**d**) Comparison of catalytic sites. Each catalytic site corresponds to the dot square above. The catalytic sites are superimposed on the corresponding catalytic sites of F_1-ATPase (PDB ID: 8HHA), which are coloured in purple.

Fig. 4 Structure and motion of the gliding machinery.

(**a**) Fitting of the atomic model of the motor into the EM map of the motor chain. The right panel shows the interface between GliDs. (**b**) Possible rotational catalytic mechanism of F_1-like ATPase. Gliγ is depicted by yellow arrows, the direction of which indicates the conformational tilt. (**c**) One possible explanation for the conversion mechanism from rotary to linear motion. Dotted arrows indicate unknown force transduction in the cell membrane. Gli349 and Gli521 are depicted in red and green, respectively. Unidentified protein regions in the gliding machinery are depicted in purple.

Acknowledgments

We acknowledge Tomomi Shimonaka at Osaka Metropolitan University and Fumiaki Makino at Osaka University for their technical assistance. This manuscript was edited using Copilot, an AI tool. This study was supported by Grants-in-Aid for Scientific

Research (A) (JP17H01544), a JST CREST grant (JPMJCR19S5) to M.M., and was supported by Research Support Project for Life Science and Drug Discovery (BINDS) from AMED under Grant Number JP22am121003 to K.N., and by JEOL YOKOGUSHI Research Alliance Laboratories of Osaka University to K.N.

Author contributions

T.T. and M.M. conceived the study. M.M. and K.N. supervised this study. T.T. prepared the cryo-EM samples and performed the biochemical analyses. J.F. and A.K. prepared the EG grid for cryo-EM observation. A.K. and T.M. performed the cryo-EM. T.T. carried out the 3D reconstruction and model building. T.K., T.H., A.K., T.M., K.K., and K.N. discussed the structural analyses. T.T. and M.M. wrote the manuscript with inputs from all authors.

Competing interests

The authors have declared no competing interest.

References

1. Stewart, A. G., Sobti, M., Harvey, R. P. & Stock, D. Rotary ATPases. *Bioarchitecture* **3**, 2–12 (2013).
2. Toyonaga, T. *et al.* Chained structure of dimeric F1-like ATPase in *Mycoplasma mobile* gliding machinery. *mBio* **12**, (2021).
3. Nishikawa, M. S. *et al*. Refined mechanism of *Mycoplasma mobile* gliding based on structure, ATPase activity, and sialic acid binding of machinery. *mBio* **10**, (2019).

4. Kobayashi, K. *et al*. Movements of *Mycoplasma mobile* gliding machinery detected by high-speed atomic force microscopy. *mBio* **12**, (2021).

5. Kühlbrandt, W. Structure and mechanisms of F-Type ATP synthases. *Annu Rev Biochem* **88**, 515–549 (2019).

6. Nakane, D. & Miyata, M. Cytoskeletal 'jellyfish' structure of *Mycoplasma mobile*. *Proc Natl Acad Sci U S A* **104**, 19518–19523 (2007).

7. Noji, H. & Ueno, H. How Does F1-ATPase Generate Torque?: Analysis From Cryo-Electron Microscopy and Rotational Catalysis of Thermophilic F1. *Front Microbiol* **13**, (2022).

8. Nakano, A., Kishikawa, J. ichi, Mitsuoka, K. & Yokoyama, K. Mechanism of ATP hydrolysis dependent rotation of bacterial ATP synthase. *Nat Commun* **14**, (2023).

9. Noji, H., Yasuda, R., Yoshida, M. & Kinosita, K. Direct observation of the rotation of F1-ATPase. *Nature* **386**, 299–302 (1997).

10. Abrahams, J. P., Leslie, A. G. W., Lutter, R. & Walker, J. E. Structure at 2.8 Å resolution of F1-ATPase from bovine heart mitochondria. *Nature* **370**, 621–628 (1994).

11. Tulum, I., Kimura, K. & Miyata, M. Identification and sequence analyses of the gliding machinery proteins from *Mycoplasma mobile*. *Scientific Reports 2020 10:1* **10**, 1–11 (2020).

12. Béven, L. *et al.* Specific evolution of F1-like ATPases in mycoplasmas. *PLoS One* **7**, e38793 (2012).

13. Bredt, W. & Radestock, U. Gliding motility of *Mycoplasma pulmonis*. *J Bacteriol* **130**, 937 (1977).

14. Rosengarten, R. & Kirchhoff, H. Gliding motility of Mycoplasma sp. nov. strain 163K. *J Bacteriol* **169**, 1891–1898 (1987).

15. Miyata, M. & Hamaguchi, T. Prospects for the gliding mechanism of *Mycoplasma mobile*. *Curr Opin Microbiol* **29**, 15–21 (2016).

16. Fujita, J. *et al.* Epoxidized graphene grid for highly efficient high-resolution cryoEM structural analysis. *Sci Rep* **13**, (2023).

17. Leimgruber, R. M. & Senior, A. E. Removal of 'tightly bound' nucleotides from phosphorylating submitochondrial particles. *Journal of Biological Chemistry* **251**, 7110–7113 (1976).

18. Menz, R. I., Walker, J. E. & Leslie, A. G. W. Structure of bovine mitochondrial F(1)-ATPase with nucleotide bound to all three catalytic sites: implications for the mechanism of rotary catalysis. *Cell* **106**, 331–341 (2001).

19. Tanigawara, M. *et al.* Role of the DELSEED Loop in Torque Transmission of F1-ATPase. *Biophys J* **103**, 970–978 (2012).

20. Sobti, M. *et al.* Cryo-EM structures of the autoinhibited *E. coli* ATP synthase in three rotational states. *Elife* **5**, (2016).

21. Kohori, A. *et al.* Torque generation in F1-ATPase devoid of the entire amino-terminal helix of the rotor that fills half of the stator orifice. *Biophys J* **101**, 188–195 (2011).

22. Bowler, M. W. Conformational dynamics in phosphoglycerate kinase, an open and shut case? *FEBS Lett* **587**, 1878–1883 (2013).

23. Rojas-Pirela, M. *et al.* Phosphoglycerate kinase: structural aspects and functions, with special emphasis on the enzyme from Kinetoplastea. *Open Biol* **10**, (2020).

24. Rao, L., Berger, F., Nicholas, M. P. & Gennerich, A. Molecular mechanism of

cytoplasmic dynein tension sensing. *Nature Communications 2019 10:1* **10**, 1–17 (2019).

25. Fukushima, M., Toyonaga, T., Tahara, Y. O., Nakane, D. & Miyata, M. Internal structure of *Mycoplasma mobile* gliding machinery analyzed by negative staining electron tomography. *Biophys Physicobiol* e210015 (2024) doi:10.2142/BIOPHYSICO.BPPB-V21.0015.

26. Nonaka, T., Adan-Kubo, J. & Miyata, M. Triskelion structure of the Gli521 protein, involved in the gliding mechanism of *Mycoplasma mobile*. *J Bacteriol* **192**, 636–642 (2010).

27. Hamaguchi, T., Kawakami, M., Furukawa, H. & Miyata, M. Identification of novel protein domain for sialyloligosaccharide binding essential to *Mycoplasma mobile* gliding. *FEMS Microbiol Lett* **366**, (2019).

28. Ibuki, T. *et al.* Common architecture of the flagellar type III protein export apparatus and F- and V-type ATPases. *Nat Struct Mol Biol* **18**, 277–282 (2011).

29. Majewski, D. D. *et al.* Cryo-EM structure of the homohexameric T3SS ATPase-central stalk complex reveals rotary ATPase-like asymmetry. *Nat Commun* **10**, (2019).

30. Miyata, M. *et al.* Tree of motility - A proposed history of motility systems in the tree of life. *Genes. Cell* **25**, 6–21 (2020).

31. Nottelet, P. *et al.* The mycoplasma surface proteins MIB and MIP promote the dissociation of the antibody-antigen interaction. *Sci Adv* **7**, (2021).

32. Aluotto, B. B., Wittler, R., Williams, C. & Faber, J. Standardized bacteriologic techniques for the characterization of *Mycoplasma* species1, 2. *Int J Syst Evol Microbiol* **20**, 35–58 (1970).

33. Miyata, M. *et al*. Gliding mutants of *Mycoplasma mobile*: relationships between motility and cell morphology, cell adhesion and microcolony formation. *Microbiology (Reading)* **146 (Pt 6)**, 1311–1320 (2000).

34. Uenoyama, A., Seto, S., Nakane, D. & Miyata, M. Regions on Gli349 and Gli521 protein molecules directly involved in movements of *Mycoplasma mobile* gliding machinery, suggested by use of inhibitory antibodies and mutants. *J Bacteriol* **191**, 1982–1985 (2009).

35. Mizutani, M., Tulum, I., Kinosita, Y., Nishizaka, T. & Miyata, M. Detailed analyses of stall force generation in *Mycoplasma mobile* gliding. *Biophys J* **114**, 1411–1419 (2018).

36. Hellman, U., Wernstedt, C., Góñez, J. & Heldin, C. H. Improvement of an 'In-Gel' digestion procedure for the micropreparation of internal protein fragments for amino acid sequencing. *Anal Biochem* **224**, 451–455 (1995).

37. Fujita, J. *et al.* Structures of a FtsZ single protofilament and a double-helical tube in complex with a monobody. *Nat Commun* **14**, (2023).

38. Mastronarde, D. N. Automated electron microscope tomography using robust prediction of specimen movements. *J Struct Biol* **152**, 36–51 (2005).

39. Punjani, A., Rubinstein, J. L., Fleet, D. J. & Brubaker, M. A. cryoSPARC: algorithms for rapid unsupervised cryo-EM structure determination. *Nat Methods* **14**, 290–296 (2017).

40. Zivanov, J. *et al*. A Bayesian approach to single-particle electron cryo-tomography in RELION-4.0. *Elife* **11**, (2022).

41. Bepler, T., Kelley, K., Noble, A. J. & Berger, B. Topaz-Denoise: general deep denoising models for cryoEM and cryoET. *Nat Commun* **11**, (2020).

42. Jumper, J. *et al.* Highly accurate protein structure prediction with AlphaFold. *Nature* **596**, 583–589 (2021).

43. Šali, A. & Blundell, T. L. Comparative protein modelling by satisfaction of spatial restraints. *J Mol Biol* **234**, 779–815 (1993).

44. Pettersen, E. F. *et al.* UCSF Chimera--a visualization system for exploratory research and analysis. *J Comput Chem* **25**, 1605–1612 (2004).

45. Emsley, P., Lohkamp, B., Scott, W. G. & Cowtan, K. Features and development of Coot. *Acta Crystallogr D Biol Crystallogr* **66**, 486–501 (2010).

46. Afonine, P. V. *et al.* Real-space refinement in PHENIX for cryo-EM and crystallography. *Acta Crystallogr D Struct Biol* **74**, 531–544 (2018).

47. Liebschner, D. *et al.* Macromolecular structure determination using X-rays, neutrons and electrons: recent developments in Phenix. *Acta Crystallogr D Struct Biol* **75**, 861–877 (2019).

48. Pintilie, G. *et al.* Measurement of atom resolvability in cryo-EM maps with Q-scores. *Nat Methods* **17**, 328–334 (2020).

49. Yamashita, K., Palmer, C. M., Burnley, T. & Murshudov, G. N. Cryo-EM single-particle structure refinement and map calculation using Servalcat. *Acta Crystallogr D Struct Biol* **77**, 1282–1291 (2021).

50. Pettersen, E. F. *et al.* UCSF ChimeraX: Structure visualization for researchers, educators, and developers. *Protein Science* **30**, 70–82 (2021).

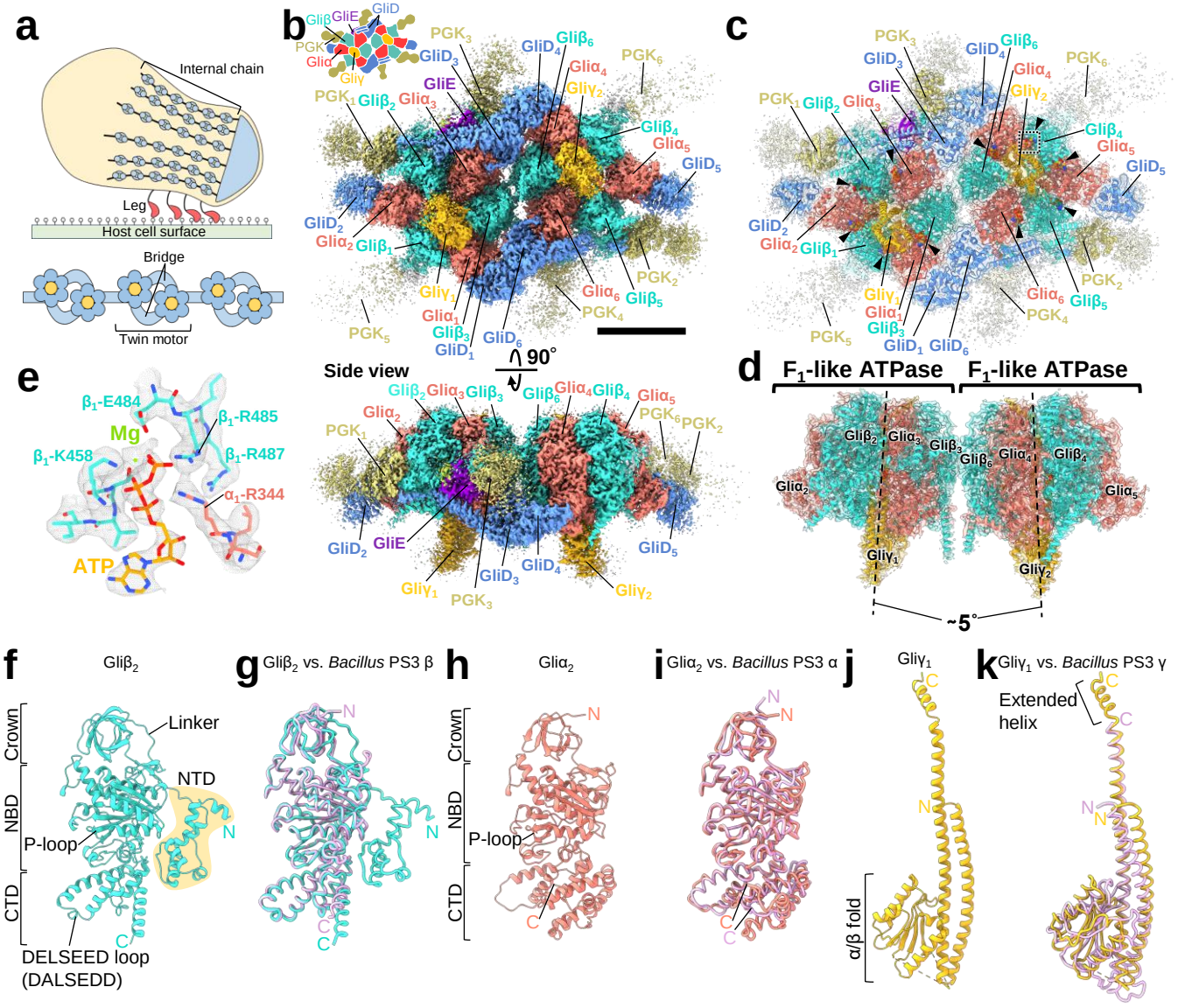
a
Internal chain
Leg
Host cell surface
Bridge
Twin motor
b
Side view
90°
c
d
F1-like ATPase
F1-like ATPase
~5°
e
β1-E484
β1-R485
Mg
β1-K458
β1-R487
α1-R344
ATP
f
Gliβ2
Linker
NTD
Crown
NBD
CTD
P-loop
DELSEED loop
(DALSEDD)
g
Gliβ2 vs. Bacillus PS3 β
h
Gliα2
i
Gliα2 vs. Bacillus PS3 α
j
Gliγ1
α/β fold
k
Gliγ1 vs. Bacillus PS3 γ
Extended
helix

Fig. 1

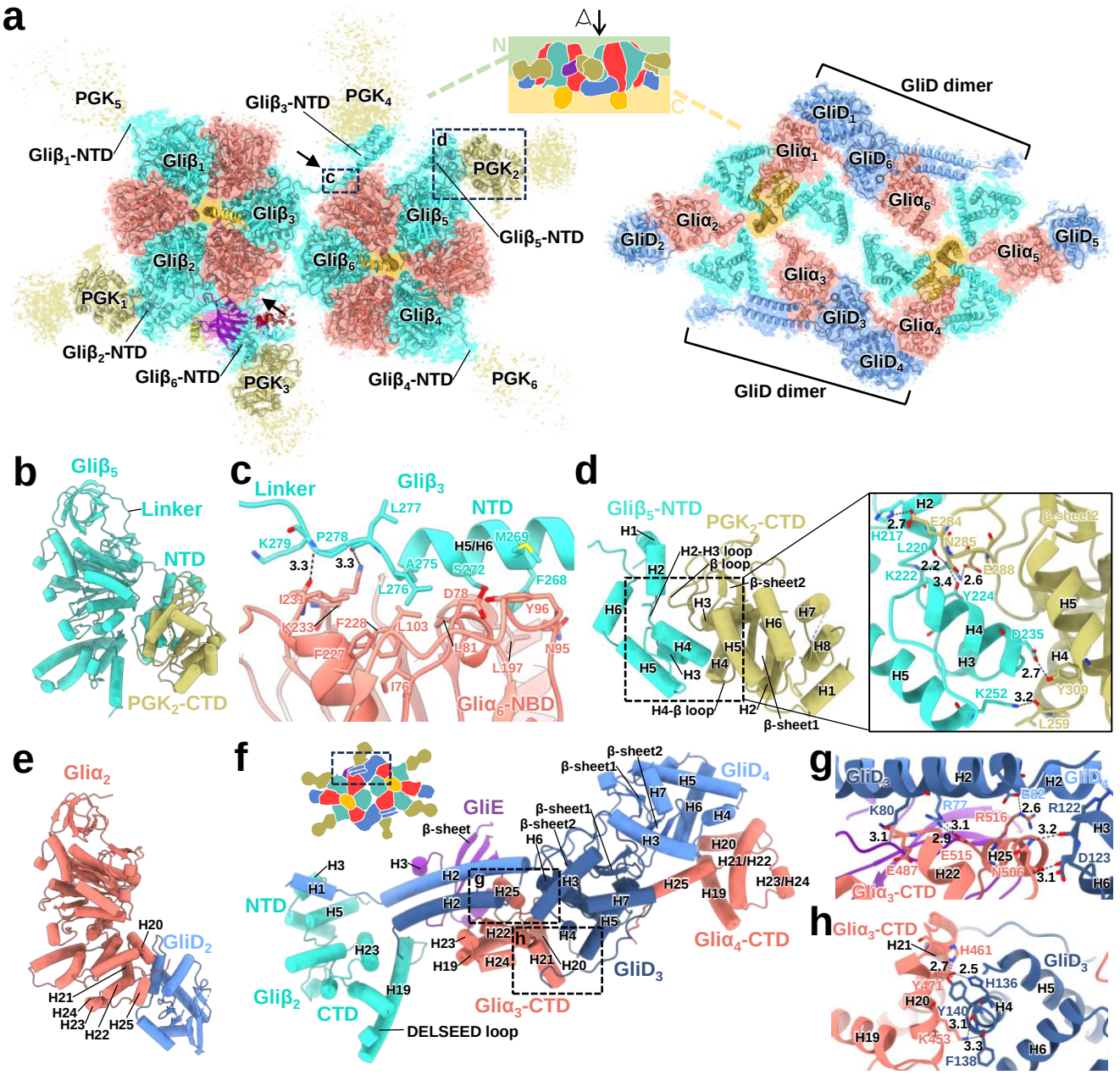
a
PGK5
Gliβ1-NTD
Gliβ1
Gliβ3-NTD
PGK4
c
d
PGK2
Gliβ3
Gliβ5
Gliβ5-NTD
Gliβ2
Gliβ6
PGK1
Gliβ4
Gliβ2-NTD
Gliβ6-NTD
PGK3
Gliβ4-NTD
PGK6
N
C
GliD dimer
GliD1
Gliα1
GliD6
Gliα6
Gliα2
GliD2
Gliα5
GliD5
Gliα3
GliD3
Gliα4
GliD4
GliD dimer
b
Gliβ5
Linker
NTD
PGK2-CTD
c
Linker
Gliβ3
NTD
L277
K279
P278
3.3
3.3
H5/H6
M269
A275
S272
F268
L276
D78
I231
Y96
K233
F228
L103
L81
N95
F227
L197
I76
Gliα6-NBD
d
Gliβ5-NTD
PGK2-CTD
H1
H2-H3 loop
β loop
H2
β-sheet2
H3
H6
H7
H6
H4
H5
H8
H5
H3
H4
H1
H4-β loop
H2
β-sheet1
H2
2.7
E284
β-sheet2
H217
L220
N285
2.2
K222
3.4
2.6
E288
Y224
H5
H4
D235
H3
H4
H5
2.7
K252
3.2
Y309
L259
e
Gliα2
H20
GliD2
H21
H24
H23
H22
H25
f
β-sheet2
β-sheet1
GliD4
H5
H7
H6
H4
GliE
β-sheet1
β-sheet2
β-sheet
H6
H3
H20
H21/H22
H3
H3
H2
g
H25
H3
H25
H23/H24
H1
H2
H7
H19
NTD
H5
H5
H22
h
H4
H23
H23
H19
H24
H21
H20
GliD3
Gliα4-CTD
H19
Gliβ2
CTD
Gliα3-CTD
DELSEED loop
g
GliD3
H2
H2
GliD4
E82
K80
R77
R516
2.6
R122
3.1
3.1
2.9
3.2
H3
E515
H25
D123
E487
H22
N506
3.1
H6
Gliα3-CTD
h
Gliα3-CTD
H21
H461
2.7
2.5
GliD3
Y471
H136
H5
H20
Y140
H4
3.1
H19
K453
3.3
H6
F138

Fig. 2

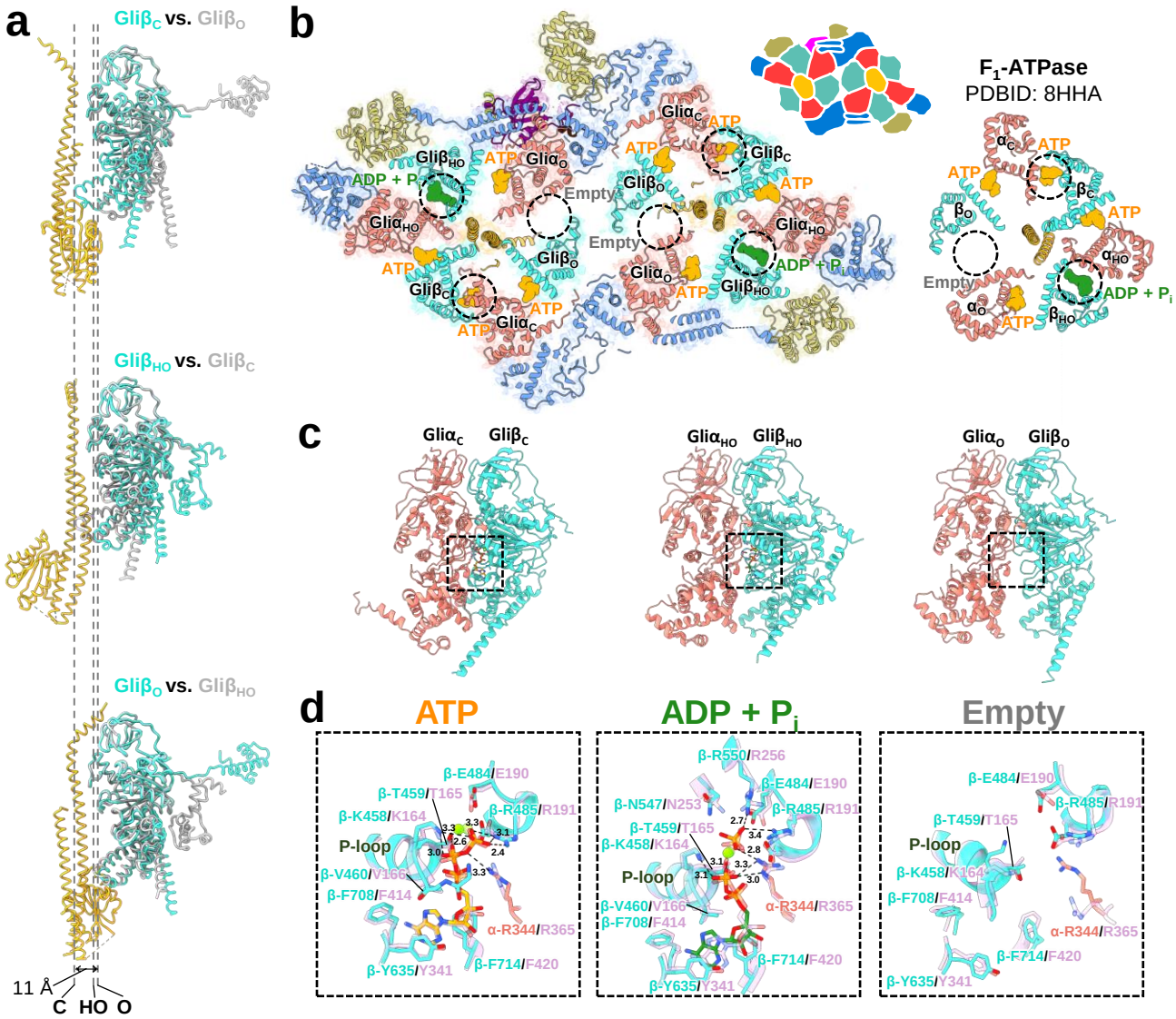
a
Gliβ$_C$ vs. Gliβ$_O$
Gliβ$_{HO}$ vs. Gliβ$_C$
Gliβ$_O$ vs. Gliβ$_{HO}$
11 Å
C HO O
b
F$_1$-ATPase
PDBID: 8HHA
Gliβ$_{HO}$
ADP + P$_i$
ATP
Gliα$_O$
Empty
Gliα$_C$
Gliβ$_C$
Gliβ$_O$
Gliα$_{HO}$
α$_C$
β$_C$
β$_O$
α$_{HO}$
α$_O$
β$_{HO}$
c
Gliα$_C$ Gliβ$_C$
Gliα$_{HO}$ Gliβ$_{HO}$
Gliα$_O$ Gliβ$_O$
d
ATP
ADP + P$_i$
Empty
β-E484/E190
β-T459/T165
β-K458/K164
β-R485/R191
P-loop
β-V460/V166
β-F708/F414
α-R344/R365
β-F714/F420
β-Y635/Y341
β-R550/R256
β-N547/N253

Fig. 3

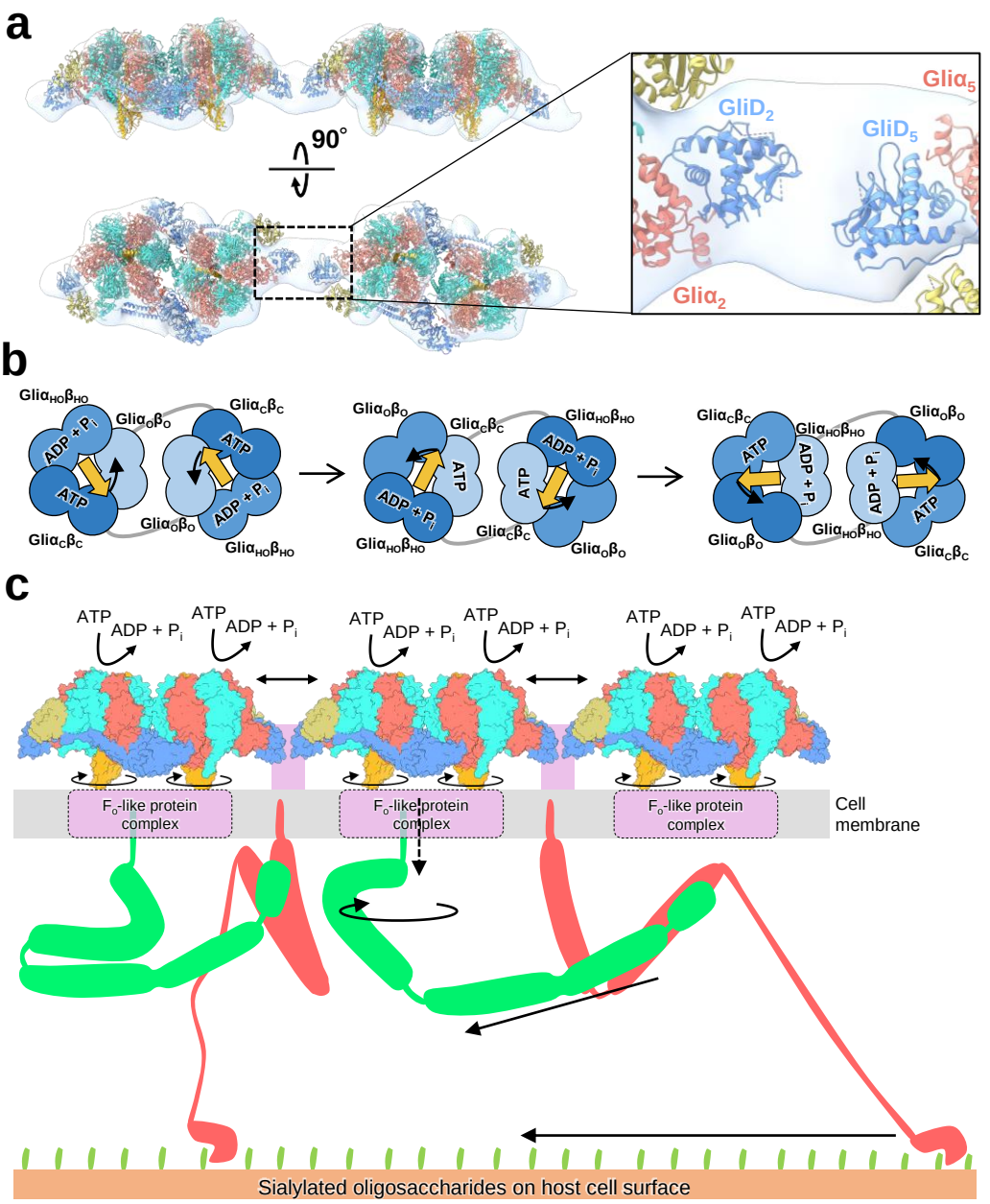
a
90°
Gliα5
GliD2
GliD5
Gliα2
b
GliαHOβHO
GliαOβO
GliαCβC
ADP + Pi
ATP
c
ATP
ADP + Pi
Fo-like protein complex
Cell membrane
Sialylated oligosaccharides on host cell surface

Fig. 4